



ELSEVIER

Available online at www.sciencedirect.com

SCIENCE @ DIRECT®

Nuclear Instruments and Methods in Physics Research A 540 (2005) 140–157

NUCLEAR
INSTRUMENTS
& METHODS
IN PHYSICS
RESEARCH
Section A

www.elsevier.com/locate/nima

Position reconstruction in drift chambers operated with Xe, CO₂ (15%)

C. Adler^a, A. Andronic^b, H. Appelshäuser^b, J. Bielcikova^a, C. Blume^c, P. Braun-Munzinger^b, D. Bucher^d, O. Busch^b, V. Cătănescu^{a,e}, M. Ciobanu^{b,e}, H. Daues^b, D. Emschermann^a, O. Fateev^f, P. Foka^b, C. Garabatos^b, T. Gunji^g, N. Herrmann^a, M. Inuzuka^g, M. Ivanov^{a,h}, E. Kislov^f, V. Lindenstruthⁱ, C. Lippmann^{b,*}, W. Ludolphs^a, T. Mahmoud^a, V. Petracek^a, M. Petrovici^c, S. Radomski^b, I. Rusanov^a, A. Sandoval^b, R. Santo^d, R. Schicker^a, K. Schwarz^b, R.S. Simon^b, L. Smykov^f, H.K. Soltveit^a, J. Stachel^a, H. Stelzer^b, G. Tsiledakis^b, B. Vulpescu^a, J.P. Wessels^d, B. Windelband^a, V. Yurevich^f, Yu. Zanevsky^f, O. Zaudtke^d

^aPhysikalisches Institut der Universität Heidelberg, Germany

^bGesellschaft für Schwerionenforschung, Planckstr. 1, D-64291 Darmstadt, Germany

^cInstitut für Kernphysik, Universität Frankfurt, Germany

^dInstitut für Kernphysik, Universität Münster, Germany

^eNIPNE Bucharest, Romania

^fJINR Dubna, Russia

^gUniversity of Tokyo, Japan

^hPH Division, CERN, Switzerland

ⁱKirchhoff-Institut für Physik, Heidelberg, Germany

Received 1 November 2004; accepted 4 November 2004

For the ALICE Collaboration
Available online 13 December 2004

Abstract

We present measurements of position and angular resolution of drift chambers operated with a Xe, CO₂ (15%) mixture. The results are compared to Monte Carlo simulations and important systematic effects—in particular the dispersive nature of the absorption of transition radiation and non-linearities—are discussed. The measurements were carried out with prototype drift chambers of the ALICE Transition Radiation Detector, but our findings

*Corresponding author. Tel.: +49 6159 71 1341; fax: +49 6159 71 2155.

E-mail address: c.lippmann@gsi.de (C. Lippmann).

URL: <http://www-linux.gsi.de/~lippman>.

can be generalized to other drift chambers with similar geometry, where the electron drift is perpendicular to the wire planes.

© 2004 Published by Elsevier B.V.

PACS: 29.40.Cs

Keywords: Drift chamber; ALICE; TRD; Position resolution; Angular resolution; Transition radiation

1. Introduction

Around 40 years after their introduction [1], multiwire proportional chambers (MWPCs) and drift chambers are widely in use in particle physics experiments and other fields. The main properties of these detectors, i.e. good position, timing and energy resolution and competitive rate capabilities at low cost, make them very attractive for usage in large scale high-energy physics and heavy ion experiments.

The characteristics of these detectors have been extensively studied in the past [2]. However, with the stringent requirements of modern experiments and with new applications for proportional chambers, still a large effort is devoted to the understanding and improvement of existing designs and to the development of new concepts.

In this publication, we investigate the position reconstruction capabilities of the Transition Radiation Detector (TRD) [3] of the ALICE experiment. ALICE¹ is a dedicated heavy ion experiment to be operated at the Large Hadron Collider (LHC) at CERN. The ALICE TRD offers three-dimensional tracking, electron/pion identification and—combining these two capabilities—a fast trigger on high- p_t electrons and jets. At the very high particle multiplicities anticipated in central Pb–Pb collisions (several thousand charged particles per unit of rapidity at mid-rapidity) at the LHC, these are very ambitious tasks. To be able to select stiff electron tracks, an excellent position reconstruction performance in the bending plane of the ALICE magnetic field is required, characterized by a position resolution below 400 μm and an angular resolution better than 1°.

2. The ALICE TRD

In this section we describe the transition radiation detector of the ALICE experiment, in particular its position reconstruction and particle identification capabilities.

2.1. General description and working principle

The ALICE TRD consists of 540 chambers surrounding the Time Projection Chamber (TPC) in six layers at an overall length of about 7 m. The total sensitive area is roughly 750 m²; the largest chamber is 159 cm long and 120 cm wide. Each module is about 13 cm thick, including radiator, electronics and cooling. The total anticipated radiation thickness for six layers is about $0.15X_0$.

A schematic cross-section of a TRD module is shown in Fig. 1. The gas volume is subdivided into a 3 cm drift region and a 0.7 cm amplification region, separated by a cathode wire grid with 0.25 cm wire pitch and 75 μm wire diameter. The anode wires have 0.5 cm pitch and 20 μm diameter. The drift chambers are equipped with cathode pads of varying sizes² and are read out via charge sensitive preamplifiers/shapers (PASA). The whole system will consist of about 1.18 million channels (readout pads). The maximum drift time is about 2 μs and the induced signal is sampled on all channels at 10 MHz to record the time evolution of the signal [4,5]. A typical signal generated by a particle track through a prototype drift chamber is also shown in Fig. 1.

A 4.8 cm thick radiator is placed in front of each gas volume. This radiator is a sandwich of polypropylene fibers and Rohacell foam, which

¹A Large Ion Collider Experiment.

²The width of the pads ranges from 0.664 to 0.818 cm, their length from 7.5 to 9 cm.

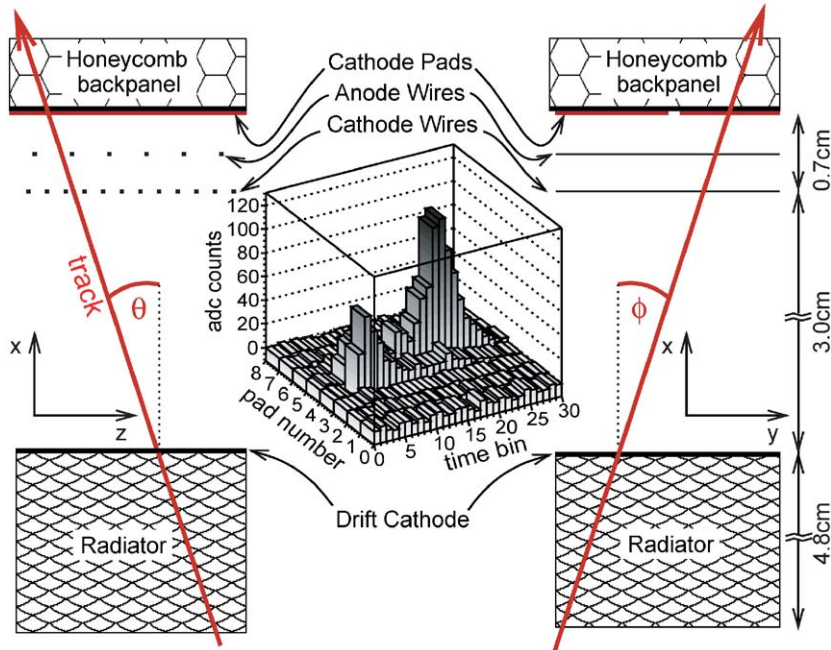


Fig. 1. Schematic view of a TRD chamber (not to scale). The left cross-section shows a projection of the chamber in the x - z plane, perpendicular to the wires, the right one shows a projection in the x - y plane, which is the bending plane of the particles in the ALICE magnetic field. A particle trajectory is also sketched. The insert shows the pulse height versus drift time on eight cathode pads for an example event. One time bin corresponds to 100 ns.

provides many interfaces between materials with different dielectric constants. Transition radiation (TR) is emitted by particles traversing the radiator with a velocity larger than a certain threshold [6], which for typical materials corresponds to a Lorentz factor of $\gamma \approx 1000$. The produced TR photons have energies in the X-ray range (1–30 keV) [7] and a high- Z gas mixture (Xe, CO₂ (15%)) is used to provide efficient absorption of these photons.

2.2. Electron identification

The TRD will provide electron identification for momenta above 1 GeV/ c [8]. To discriminate electrons from the large background of pions two characteristic phenomena are used:

- (i) The ionization energy loss [9] at the momentum region of interest is larger for electrons than for pions, since here electrons are at the

plateau of ionization energy loss, while pions are minimum ionizing or on the relativistic rise.

- (ii) In the momentum range considered, only electrons exceed the TR production threshold.

Fig. 2 shows the mean pulse height as a function of the drift time for pions and electrons [4]. Here, and in the following, the time zero is arbitrarily shifted to facilitate a simultaneous measurement of the baseline and of noise. Due to the larger ionization energy loss at these specific conditions ($p = 2$ GeV/ c) the mean signal is about 40% larger in the case of electrons (without radiators). With radiators the energy deposited by absorbed TR photons contributes considerably to the mean amplitude of the electrons. The characteristic signal shape for electrons with radiators is determined by the exponential probability distribution for the absorption of TR photons in the gas mixture.

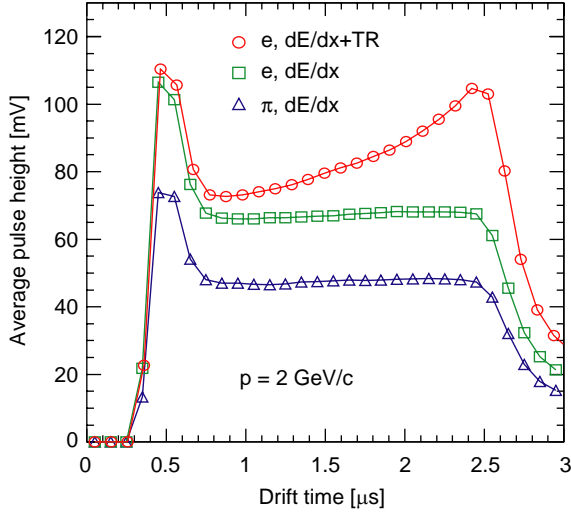


Fig. 2. Measured average pulse height as a function of the drift time for pions and electrons (with and without radiator). The peak at short drift times is due to the fact that electrons produced by ionization in the amplification region drift towards the anode wires from both sides of the wire plane, which leads to an approximate doubling of the average pulse height. In general, the average pulse height is larger for electrons. TR adds a significant energy deposit and introduces the characteristic signal shape of electrons, determined by the exponential absorption probability distribution of TR photons in the gas.

2.3. Tracking

In this publication, we focus on the position reconstruction performance of the ALICE TRD in the bending plane of the particles in the ALICE magnetic field, which is parallel to the wires of the TRD and to the electric drift field. This defines the transverse momentum resolution of the TRD. In the third dimension, parallel to the magnetic field lines, the resolution is limited by larger pads and by the discrete wire positions. A tilted-pad design will be employed to increase the tracking capabilities in this direction.

An example event in a TRD chamber is shown in Fig. 3. From the pulse height distribution on eight adjacent pads of 0.75 cm width, the cluster position is reconstructed as a function of the drift time. In this context a cluster represents electrons triggering avalanches in a given time bin. For a discussion of the position reconstruction method see Section 5.3. Electrons generated close to the

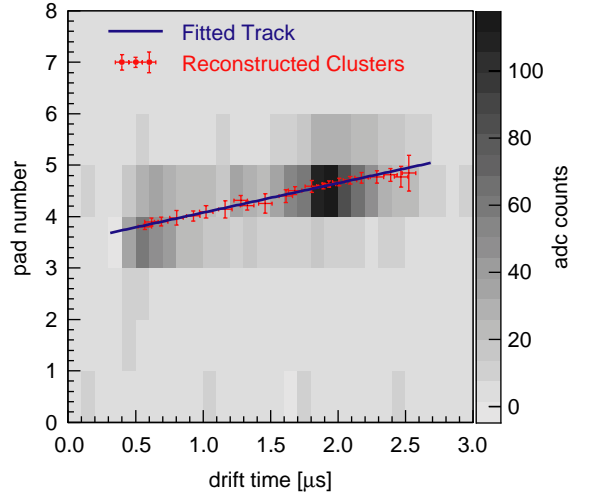


Fig. 3. Same example event as in Fig. 1. The reconstructed clusters and a fitted track are overlaid.

anode wire grid have a small drift time and induce signals corresponding to a small time bin number. Electrons originating close to the drift electrode, on the other hand, have a larger drift time and thus correspond to larger time bin numbers. The drift time can be translated to a position (distance from the anode wire plane) if the drift velocity is known. For the ALICE TRD we aim for a drift velocity of around $1.5 \text{ cm}/\mu\text{s}$ in the drift region. When the clusters at all time bins are reconstructed, a straight line fit—as in Fig. 3—defines the reconstructed track. The reconstructed angle ϕ_{rec} is obtained by

$$\tan \phi_{\text{rec}} = \frac{aW}{v_{\text{D}}^{\text{av}}} \quad (1)$$

where a is the slope parameter of the linear fit line in pad units, W is the pad width in cm and v_{D}^{av} is the average drift velocity of electrons in the detector in $\text{cm}/\mu\text{s}$.

3. Experimental setup

The measurements were carried out at momenta of 1–6 GeV/c at the T10 secondary beam line at the CERN PS. A sketch of the beam setup is shown in [10]. The beam was a mixture of electrons and negative pions with a momentum spread of

about 1%. Clean samples of each particle type were selected using coincident thresholds on two Čerenkov detectors and a lead–glass calorimeter. Position reference was provided by two silicon detectors with a 50 μm strip pitch. With this silicon telescope the beam divergence was found to be around 0.1° (σ).

We tested four identical prototype drift chambers³ with a construction similar to that for the final TRD, but with a smaller active area ($25 \times 32 \text{ cm}^2$). The dimensions of the pads were $0.75 \times 8 \text{ cm}^2$. We used a prototype of the PASA with a noise on-detector of about 1000 electrons (r.m.s.). The FWHM of the output pulse is about 100 ns for an input step function. The nominal gain of the PASA is 12 mV/fC but during the present measurements we used a gain of 6 mV/fC to better match to the range of the employed Flash ADC system with 0.6 V voltage swing. The high voltage at the anode wires was adjusted to four values corresponding to gas gains of 2400, 3900, 6200 and 9600. A gain value of around 4000 is anticipated as the nominal value for the ALICE TRD.

4. Detector simulations

For simulations of the TRD performance we use AliRoot [11], the ALICE software package. AliRoot provides an object oriented framework for event simulations and reconstruction in the ALICE detector. The TRD part of AliRoot contains a full microscopic simulation of the detector physics processes. The interaction of the charged particles with the detector materials and their energy loss is simulated using Geant 3.21 [12]. Since the production of transition radiation is not included in Geant 3, it was explicitly added to AliRoot. We use a momentum dependent parameterization which applies an approximate for-

mula for the TR yield of a regular stack of foils with fixed thickness, including absorption [3,13].

The energy transfers in primary collisions and the energy deposited by TR are converted into a number of secondary electrons and the electron collection is simulated taking into account electron drift and diffusion, amplification fluctuations, the distribution of the induced charge on the cathode pads (pad response), the time response of the detector (ion tail) as well as that of the electronics, and finally noise. The deposited charge is translated into raw-data-like ADC signals which then serve as input for track reconstruction.

In this publication we use AliRoot to study in some detail the different contributions to the position reconstruction performance of the ALICE TRD. During our studies some changes had to be made in the AliRoot code, which will be described in the following.

4.1. Transition radiation absorption

TR photons are emitted in the radiator with an angular distribution about the direction of the emitting particle, which is sharply peaked at $1/\gamma$ [6]. As a consequence, the TR photons cannot be separated from the incident electron track and contribute to the tracking information. The drift chamber detects the photoelectron ejected from a gas atom and the charge that is released by the secondary processes. This can introduce a considerable smearing of charge deposit and hence a degradation of the tracking performance of the detector.⁴

In the following, we only consider the xenon atoms; photon interactions with CO_2 atoms are neglected. In the absorption process, a photoelectron of energy $E_e = E_X - E_S$ is created, where E_X is the energy of the TR photon and E_S is the binding energy of the photoelectron.⁵ At the relevant X-ray energies, the photoelectron is emitted preferentially in a plane perpendicular to

³Generally, in this publication we will average over the behavior of these four chambers, thus increasing the statistics of the measurements. Only where the performance of the four chambers is expected to be different, e.g. due to the track curvature in the magnetic field, we show results for a single chamber.

⁴The physical limitations imposed on the imaging quality of a xenon-filled MWPC X-ray imaging detector are studied in detail in [14].

⁵The xenon K-shell binding energy is about 35 keV, the average L- and M-shell binding energies are about 5.1 and 0.9 keV, respectively.

the incoming photon track [15]. Even though subsequent multiple scattering and ionizing collisions with the gas molecules randomize the photoelectron trajectory, the charge will be deposited some distance away from the track. The practical range $R(E_e)$ of this electron in a gas can be calculated according to [2]

$$R(E_e) = A E_e \left(1 - \frac{B}{1 + C E_e} \right) \text{g/cm}^2 \quad (2)$$

where $A = 5.37 \times 10^{-4} \text{g cm}^{-2} \text{keV}^{-1}$, $B = 0.9815$ and $C = 3.123 \times 10^{-3} \text{keV}^{-1}$. As an example, for our gas mixture the range of a 10 keV electron is about 500 μm .

The emission of the photoelectron leaves a hole in the shell which will be filled with electrons from higher shells. This de-excitation occurs by emission of either an Auger electron or a fluorescence photon. The probability for de-excitation by photon emission is determined by the fluorescence yield, which is 0.87 for the xenon K-shell [16]. The fluorescence photon energy is $E_S - E_T$, where E_T is the binding energy of the second shell involved in the transition. The emission of fluorescence photons is isotropic and their absorption length in the gas is exponentially distributed with a mean that is given by the attenuation coefficient. As an example, a K-shell fluorescence photon will have an energy of $E_K \approx 35 \text{keV}$; in pure xenon it will have an absorption length of 24 cm and can generate a background hit at a distant position. However, since the energy of the largest part of the TR photons is below E_K , these are rare events (i.e. 1.4% at $p = 2 \text{GeV}/c$). L-shell fluorescence X-rays, on the other hand, are very common (due to the mean TR photon energies around 10 keV and the large fluorescence yield); they carry an energy of around 5 keV and have an absorption length around 0.4 cm in Xenon. Auger electron emission is also isotropic. The range of the Auger electrons is calculated by Eq. (2). As an example, an Auger electron emerging from the L-shell ($E_K - 2E_L \approx 25 \text{keV}$) has a range around 0.2 cm in Xenon. A simplified picture of the just described secondary processes has been added to the AliRoot code to allow studies of their influence on the position reconstruction performance of the TRD.

4.2. Electron drift path

In drift chambers one takes advantage of a unique relation between the position of primary ionization electrons (x) and the drift time (t_D) to the nearest anode wire, where the electrons generate avalanches. To precisely reconstruct the position of the passage of the particle through the detector one generally wants to know this space–time relation, which may not be linear

$$x = \int_0^{t_D} v_D(t) dt. \quad (3)$$

Here $v_D(t)$ is the local drift velocity at time t . For constant drift velocity the space–time relation Eq. (3) becomes linear

$$x = v_D t_D. \quad (4)$$

In the TRD v_D is constant in a large fraction of the detector ($v_D = v_0 = 1.5 \text{cm}/\mu\text{s}$ in the drift region), but (in general) higher in the amplification region. However, one can approximate

$$x \approx v_D^{\text{av}} t_D \quad (5)$$

where v_D^{av} is an average drift velocity. We used GARFIELD [17] to calculate drift times t_D (Fig. 4a) and average drift velocities v_D^{av} (Fig. 4b) for electrons generated at a given (x, z') position. Here z' denotes the lateral distance of the position of the drifting electrons to the closest anode wire ($0 \leq z' \leq 0.25 \text{cm}$). A large number of electrons were drifted from each position (including diffusion) and the most probable drift time was taken. We find that v_D^{av} is approximately equal to v_0 only close to the drift cathode ($x \approx 3.35 \text{cm}$), but increases as x decreases. In the amplification region it is in general more than twice as large (3.5 cm/ μs).

However, the drift time t_D depends also on z' . Fig. 5 shows the different drift paths for electrons coming from the drift region at different z -positions. At a given distance from the anode wire plane (which is situated at $x = 0 \text{cm}$), the shortest drift time is given by electrons drifting at $z' = 0 \text{cm}$. Electrons drifting at $z' = 0.25 \text{cm}$ have a longer drift path and—on top of that—cross the low field region between two anode wires. Consequently, we observe in Fig. 4a a drift time offset

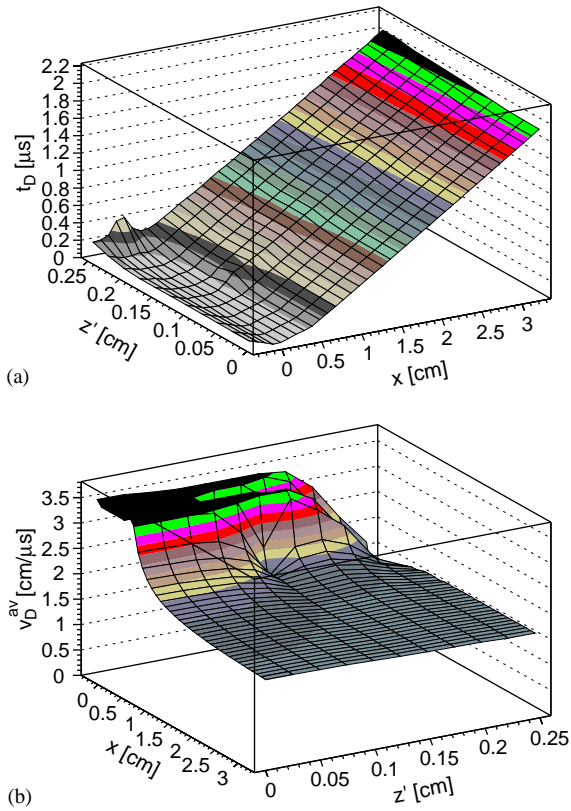


Fig. 4. (a) Average drift time t_D for electrons at different positions in the drift volume. The anode wire is situated at ($x = 0$ cm, $z' = 0$ cm). z' is the distance to the nearest anode wire in z (Figs. 1 and 5). The calculation was done with GARFIELD for the Xe, CO₂ (15%) gas mixture, an anode wire voltage of 1550 V and a drift voltage of -1950 V. (b) Corresponding distribution of the average drift velocity. Note that the coordinate system has been rotated as compared to (a) for better visibility.

depending on z' . For electrons coming from the drift cathode ($x \approx 3.35$ cm) it is around 120 ns as compared to the value at ($x = 0$ cm, $z' \approx 0$ cm). For electrons originating in the low field region at ($x = 0$ cm, $z' = 0.25$ cm) we find $v_D^{\text{av}} < 1$ cm/ μ s, resulting in a drift time offset⁶ upto 430 ns!

The non-linearity of the space–time relationship as illustrated in Fig. 4 has been added to the AliRoot code.

⁶Diffusion considerably broadens the drift time distributions, especially in this region. Fig. 4 only shows the most probable drift times.

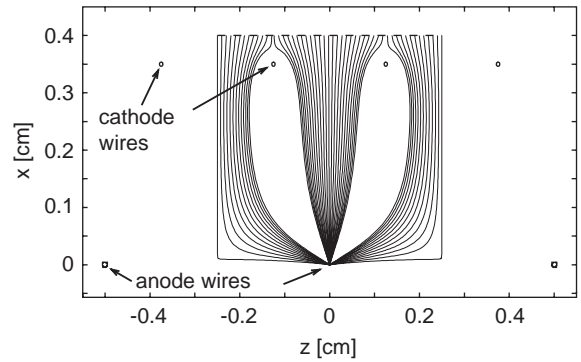


Fig. 5. Ideal drift lines for electrons coming from the drift region (from the top) at different z positions. The anode wire plane is at $x = 0$ cm; the cathode wire plane is at $x = 0.35$ cm.

4.3. Pad response function

Proportional chambers often feature a cathode plane subdivided into separate strips or—like the ALICE TRD—pads with independent charge sensitive readout for the purpose of localizing the avalanche with a precision that is a fraction of the strip or pad width W . A parameter that strongly influences the distribution of the induced charge on the cathode plane is the angular position of the avalanche at the anode wire [18]. However, in most practical situations it is not possible or desirable to restrict or control this quantity so that one generally observes a resultant effect due to all avalanche angles. There exists an empirical formula for the induced charge distribution $\rho(y)$ by Mathieson [19] that describes well such average behaviour in symmetric MWPCs along the anode wires.⁷ The coordinate y is given by the wire direction (Fig. 1).

The pad response function (PRF) $P(y)$ is obtained by integration of $\rho(y)$ over the width of the strip or pad

$$P(y) = \int_{y-W/2}^{y+W/2} \rho(y') dy'. \quad (6)$$

The ALICE TRD, however, is not exactly a MWPC, but is extended by a drift volume that is separated from the amplification volume by a

⁷A symmetric MWPC consists of a plane of anode wires centered between two planar cathodes.

cathode wire grid. As we shall see in this section, the Mathieson formula can nevertheless be used to calculate $P(y)$ for this design to a rather good accuracy.

The exact PRF $P(y)$ can be obtained by employing the weighting field formalism. The weighting field $\vec{E}_W(y)$ is the (imagined) electric field in the detector when the readout electrode is set to 1 V while all other electrodes are grounded. The field $\vec{E}_W(y)$ is generally used to calculate induced currents in arbitrary electrode geometries, using the Ramo theorem⁸ [20] via

$$i(t) = -q\vec{E}_W(\vec{r}(t)) \cdot \vec{v}(t). \quad (7)$$

The current i that is induced on a readout electrode at time t by a charge q moving with velocity \vec{v} is proportional to the weighting field \vec{E}_W at the position \vec{r} of the charge. Calculating \vec{E}_W as a function of y on the cathode plane yields the cathode charge distribution $\rho(y)$ for a given geometry. From this we can then calculate $P(y)$ following Eq. (6).

We used GARFIELD to calculate $\rho(y)$ for the ALICE TRD geometry (Fig. 6). Since we are—as already mentioned—not interested in the influence of the angular position of the avalanche around the anode wire, we average over many angles.

The exact method confirms that the Mathieson formula is a good approximation. In general, the PRF can be well approximated by a Gaussian curve [2]. The standard deviations σ_P of Gaussian fits to the $P(y)$ (in pad units) are 0.495 and 0.496 for the measured PRF and the exact calculation for the ALICE TRD geometry, respectively. For the Mathieson formula and for the exact calculation for a MWPC geometry with similar parameters⁹ we find 0.482 and 0.485, respectively. The PRF for a symmetric MWPC is narrower by about 3% (in σ_P) as compared to the TRD geometry, for our specific wire diameters, wire pitches and anode–cathode separation. The PRFs calculated with GARFIELD, as described in this section, are used for the simulation of the pad response in AliRoot.

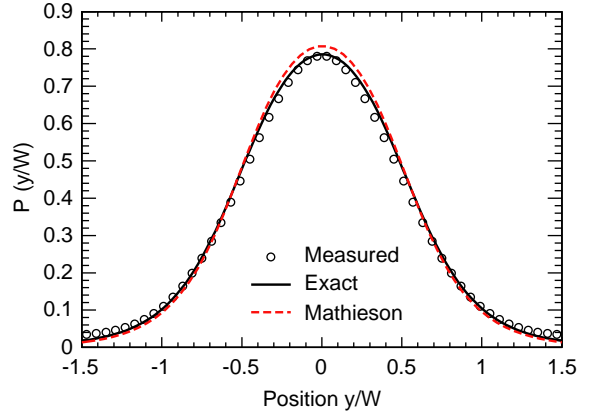


Fig. 6. Pad response functions for $W = 0.75$ cm. The circles show the measured PRF, the dashed line shows the results of a calculation using the Mathieson formula and the solid line shows the exact calculation for the ALICE TRD geometry.

5. Position reconstruction and systematic effects

In this section we present some first results on the position reconstruction performance of the ALICE TRD and describe the different systematic effects.

5.1. Definitions of resolutions

The residuals for a given track are defined as the distance between the position of the reconstructed cluster $(y_t)_{cl}$ and the position of the reconstructed track $(y_t)_{fit}$ for each time bin t

$$\Delta_y = (y_t)_{cl} - (y_t)_{fit}. \quad (8)$$

As the position resolution σ_y of the detector we define the sigma of a Gaussian fit (within 3σ) to the distribution of residuals Δ_y for a large number of tracks. This resolution does not depend on ‘external effects’ like multiple scattering in front of the gas volume of the drift chamber and/or beam divergence. It thus represents the detector-intrinsic position resolution. As the angular resolution we define the width σ_ϕ of a Gaussian fit (within 3σ) to the distributions of the reconstructed angles. This resolution includes the mentioned external effects.

⁸Also known as the reciprocity theorem.

⁹No drift region.

5.2. Tail cancellation

The signals that are read out from the cathode pads are induced by the positive ions generated in the electron avalanches near the anode wires. Since the massive ions move slowly compared to the electrons, the signals exhibit long tails. Convolution with the response of the PASA yields the time response function (TRF), which is asymmetric. For our specific chamber geometry and electronics, the tail of the TRF can be well approximated by the sum of two exponential functions with characteristic decay times

$$T_{\text{short}} \approx 0.10 \mu\text{s} \quad \text{and} \quad T_{\text{long}} \approx 0.93 \mu\text{s}. \quad (9)$$

The TRF gives rise to a strong correlation between the signal amplitude in subsequent time bins. This is in general a problem also in other related detectors, in particular in TPCs, since it biases the position measurement results as a function of time. In the case of the TRD the correlations affect especially the angle measurement (see Fig. 3). A way to minimize the effect is to remove the tails from the data by deconvolution (tail cancellation). Three different methods are studied here:

- The one exponential tail cancellation (Exp1TC) subtracts the tail (for each time bin) as a function of time. Here the tail is assumed to be a one exponential function with decay time T_{long} .
- The two exponential tail cancellation (Exp2TC) subtracts accordingly a tail that is assumed to consist of a superposition two exponential functions with decay times T_{long} and T_{short} .
- Finally we also apply a signal symmetrization (TM+TC) that first replicates the tail with T_{short} at the times preceding the maximum (tail maker, TM) and then subtracts only the long component similar to the first mentioned method (TC).

The effects of the three different methods on the TRF are shown in Fig. 7. The tail of the original TRF is largely reduced by the Exp1TC method and the maximum signal amplitude is lowered by around 10%. However, the TRF is not fully symmetrized, so we expect some correlation to

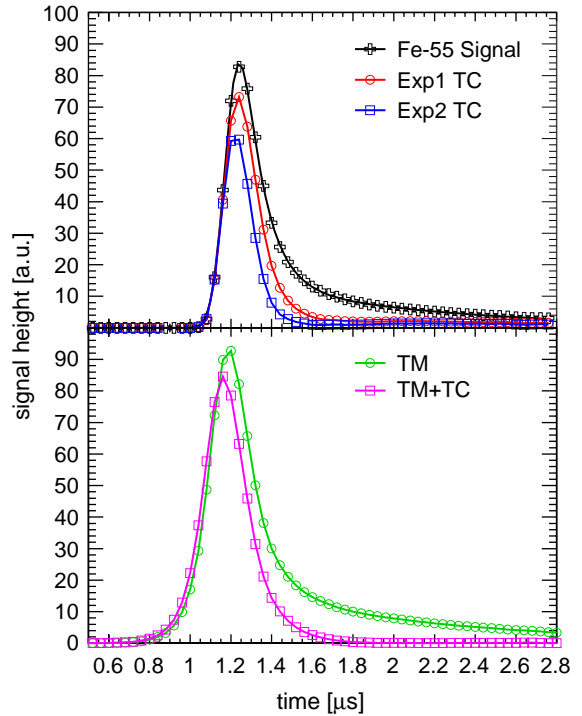


Fig. 7. Time dependence of the average PASA pulse height for ^{55}Fe X-rays. Due to the pointlike charge deposit by X-rays this signal is almost identical to the time response function (TRF). In what is shown signal diffusion is included, in the TRF it is not. The upper panel shows the original signal and the signal after applying a tail cancellation with one and two exponential functions (Exp1TC, Exp2TC). The lower panel shows the effect of adding the short tail component to the left (tail maker, TM), and of subsequent tail cancellation (long component).

remain, if this method is used. The Exp2TC method symmetrizes the TRF but the effective signal amplitude is reduced by around 30%, which introduces a considerable degradation in the signal-to-noise ratio. The TM+TC method also symmetrizes the TRF but without the drawback of a reduction in signal amplitude.

Fig. 8 shows example histograms of the residuals Δ_y of fitted tracks and of the reconstructed angles for the different tail cancellation methods described in Section 5.2. The incident angle of the beam was $\phi \approx 15^\circ$. If no tail cancellation is applied, the distributions are very broad, with pronounced tails as a result of the mentioned correlations. Since an entry at a given time bin increases the amplitude at later time bins on the

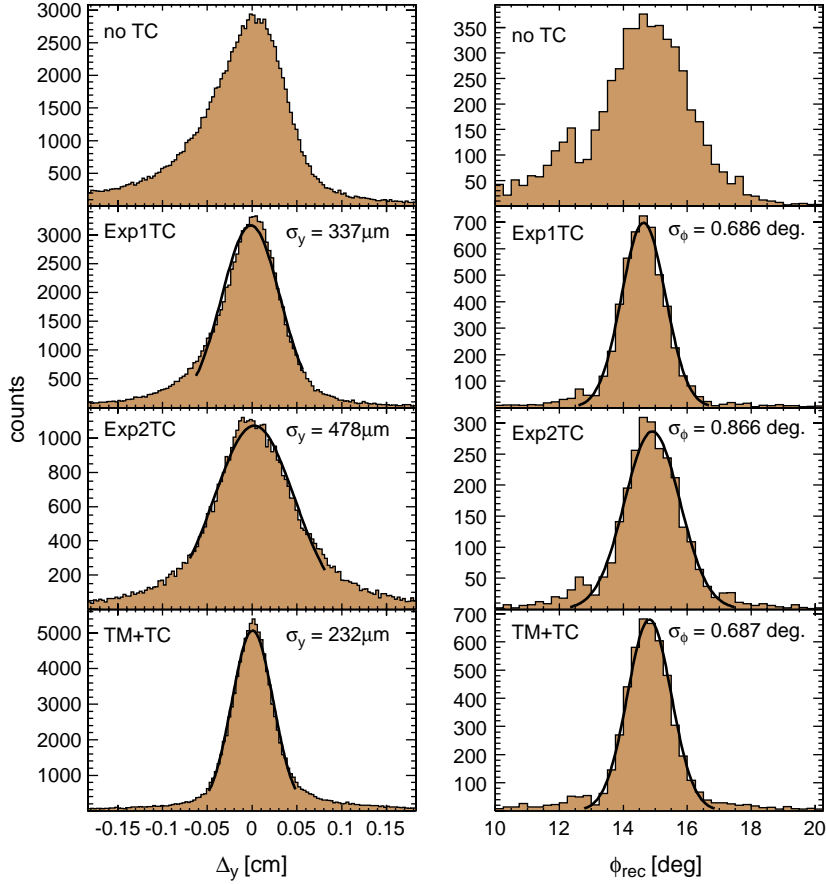


Fig. 8. Measured histograms of residuals Δy , (left panels) and of the reconstructed angles (right panels) for 6 GeV/c pions. We show data without tail cancellation and for the Exp1TC, Exp2TC and TM+TC methods (from top to bottom). Where applicable, Gaussian fits are also shown.

same pad through the TRF, the reconstructed angles are generally shifted towards smaller values by this effect. Tail cancellation improves the situation but in the case of the Exp1TC method the correlation is not fully removed. However, the correlations are nicely removed by the Exp2TC and TM+TC methods.

The best results at the described conditions are obtained using the TM+TC method ($\sigma_y = 232 \mu\text{m}$ and $\sigma_\phi = 0.687^\circ$). With the Exp1TC method we find $\sigma_y = 337 \mu\text{m}$ and $\sigma_\phi = 0.686^\circ$.

For N_{fit} independent fitpoints the relation between the accuracy of the measurement in y of the single points (here represented by σ_y) and of

the angular resolution σ_ϕ is given by [2]

$$\sigma_\phi \approx \sqrt{\frac{12}{N_{\text{fit}}}} \frac{\sigma_y}{D} \text{ rad.} \quad (10)$$

Following Eq. (10), we expect for about $N_{\text{fit}} = 20$ fitpoints (see Fig. 3), for a detector thickness of 3.7 cm and for a position resolution of $\sigma_y = 337 \mu\text{m}$ —as measured with the Exp1TC method—an angular resolution of $\sigma_\phi = 0.4^\circ$. For the TM+TC method we expect an even better angular resolution: $\sigma_\phi = 0.23^\circ$. The measured angular resolution does not reach these expected numbers. We conclude that the fitpoints are not independent as presumed by Eq. (10), since the

different correction methods supposedly do not remove fully the correlations between the signals in subsequent time bins (between the fitpoints).

5.3. Cluster reconstruction

For each time bin charge sharing between adjacent pads allows to reconstruct the position of the clusters along a pad row (in the wire direction). To calculate the y -position of that cluster (Fig. 1) we assume a Gaussian PRF.¹⁰ The amplitudes in at least two neighboring pads are required to be above threshold, which is determined by the value of the noise N . N was extracted from the baseline in the presamples of the drift chamber signals. Gaussian fits to the noise distributions yield values of around 1.7 ADC channels. The displacement y_{dis} of the cluster from pad i is calculated using a weighted mean of two measurements [2]

$$y_{\text{dis}} = \frac{1}{w_1 + w_2} \left[w_1 \left(\frac{\sigma_P^2}{W} \ln \frac{A_i}{A_{i-1}} - \frac{W}{2} \right) + w_2 \left(\frac{\sigma_P^2}{W} \ln \frac{A_{i+1}}{A_i} + \frac{W}{2} \right) \right]. \quad (11)$$

Here σ_P is the Gaussian width of the PRF, W is the pad width and w_1 , w_2 are weights: $w_1 = (A_{i-1})^2$, $w_2 = (A_{i+1})^2$, with A_i being the amplitude on pad i . The error of the cluster position is given by

$$\sigma_t = 50 \text{ ns} \quad \text{in time direction and} \quad (12a)$$

$$\sigma_y = \sqrt{(\sigma_0)^2 + \frac{2}{A^2}} \text{ cm} \quad \text{along } y. \quad (12b)$$

Here $A = A_{i-1} + A_i + A_{i+1}$ is the sum of the amplitudes on the three pads, with $A_i > A_{i-1}$ and $A_i > A_{i+1}$. The parameter $\sigma_0 \approx 0.03$ cm is a specific resolution that is optimized for the best detector performance. It is of the order of the residuals Δ_y . We also apply a center of gravity correction to the time coordinate (x in Fig. 1), by moving the reconstructed clusters in that coordinate according to the values of the amplitudes in the neighboring

¹⁰A simpler method is to calculate the center of gravity on three pads, but the PRF method yields results that are more accurate by about 10%.

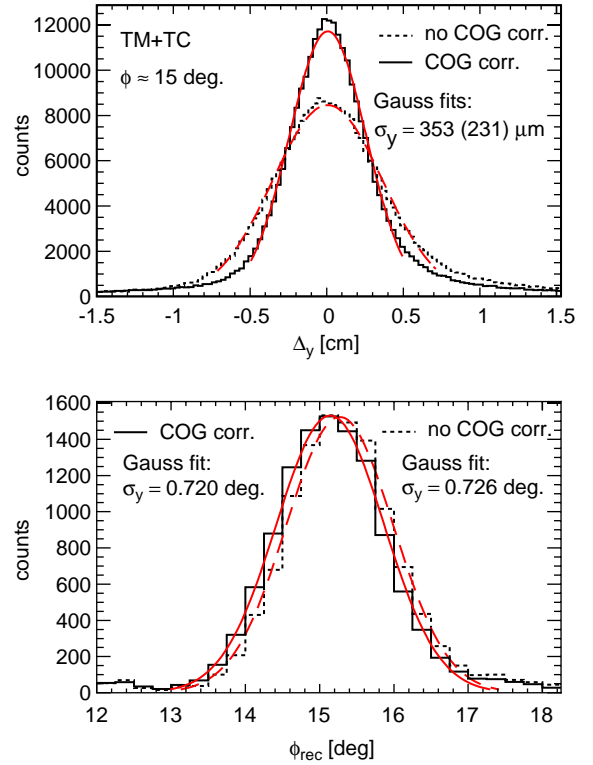


Fig. 9. Measured histograms of residuals Δ_y (top panel) and of reconstructed angles (lower panel). We compare data with (solid lines) and without (broken lines) time center of gravity correction (COG corr.).

time bins. Assuming on a given pad the three amplitudes A_{t-1} , A_t and A_{t+1} at three subsequent time bins, the cluster at time bin number t is shifted to

$$t + \delta t = t + \delta_0 \frac{-A_{t-1} + A_{t+1}}{A_{t-1} + A_t + A_{t+1}}. \quad (13)$$

$\delta_0 \approx 1.5$ is a factor that is optimized for best detector resolution.¹¹ This procedure corrects for the ambiguity of the position of the signal within the 100 ns time bins and significantly improves the position resolution: From Fig. 9 we find an improvement of 35%. Despite the better position

¹¹Since now the distance in time direction between reconstructed clusters is not constant anymore, it seems necessary to change the value of the error σ_t given by Eq. (12a) However, the effect on the resolution obtained is small and we keep σ_t constant, as in Eq. (12a). The result of the time center of gravity correction can be seen in Fig. 3.

resolution, the angular resolution is improved by only 1%. Following Eq. (10) this would again imply that to some extent the correlations between the signals in subsequent time bins cannot be removed. The obtained angular resolutions seem to be the lowest limit.

5.4. Non-linearities

Fig. 10 shows the systematic variation of the reconstructed angle ϕ_{rec} with the z -coordinate across the wires, extracted from the silicon strip detectors. Clearly visible is the influence of the anode wire grid with 0.5 cm periodicity. This systematic effect can be approximately reproduced by the simulation and is explained by the non-linearities in the time–space relationship as discussed in Section 4.2. A small variation of the angle θ from zero has to be assumed (here $\theta = 1.5^\circ$), indicating a slight misalignment of the chamber with respect to the beam. In fact, the precision of the alignment in this direction was of this order. If this is the case, the lateral distance of electrons deposited along the tracks from the nearest anode wire in the drift cell (z' in Fig. 4) is varying with the distances from the anode wire plane x . Thus an offset that depends on x is added

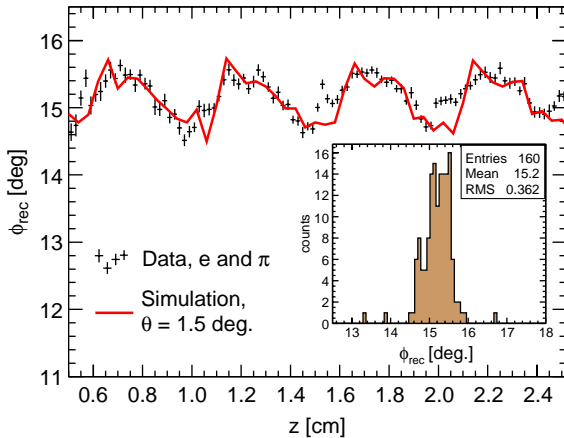


Fig. 10. Systematic variation of the reconstructed angle ϕ_{rec} with the z -coordinate (across the wires). We show measured (crosses) and simulated results (solid line). The inset shows a projection of the measured data on the ordinate, giving the overall effect due to non-linearity. The TM+TC method was used.

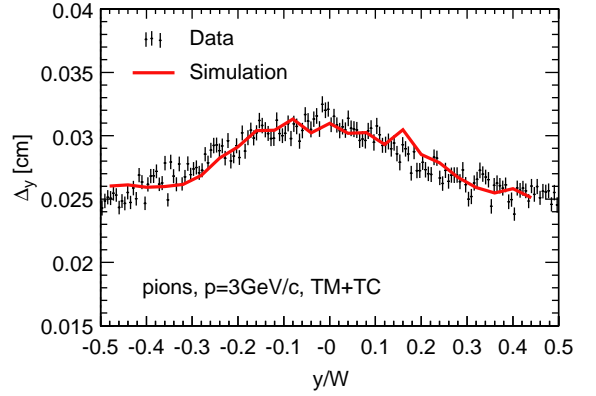


Fig. 11. Residuals Δ_y of the fit as a function of the position of the avalanche with respect to the pad. We show measured (crosses) and simulated results (solid line). The TM+TC method was used. W is the pad width.

to the drift time of the electrons, introducing the observed systematic effect. The resolution deterioration due to this effect is about 0.36° , at these specific conditions (pions, 3 GeV/c, $\phi \approx 15^\circ$). For $\theta = 0^\circ$ the systematic effect disappears in the simulated data.

Fig. 11 shows the residuals Δ_y as a function of the position of the avalanche with respect to the pad. This value is a measure of the error of the coordinate measurement using Eq. (11). For avalanches in the center of a pad the error in the measurement is about 20% larger. Since the same reconstruction method is used in the simulations, this effect is also well reproduced.

6. Position and angular resolution

Here we present the measured detector performance and compare it to AliRoot simulations.

6.1. Dependence on S/N

In this section we study the performance of the detector as a function of S/N . The signal height S was extracted from pulse height spectra (mean value) at a given time bin corresponding to the center of the drift region ($1.6\mu\text{s}$ drift time at nominal conditions as in Fig. 2).

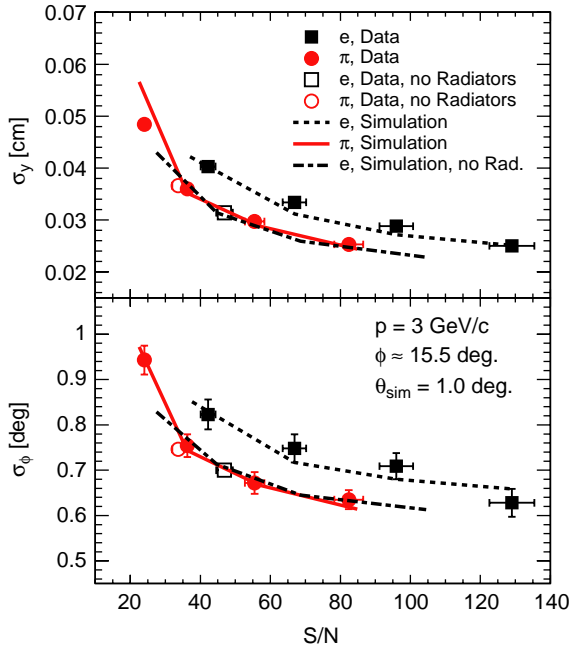


Fig. 12. Position resolution σ_y and angular resolution σ_ϕ as a function of the signal-to-noise ratio (S/N). The filled squares (circles) show the measured data for four different gain values for electrons (pions) with radiators in front of the drift chambers. The large open squares (circles) show the measured data for electrons (pions) with no radiators and for one given gain. The lines show simulation results for different gains for pions and electrons with and without radiators.

The dependence of σ_y and σ_ϕ on S/N is shown in Fig. 12. Again the incident angle of the beam was about $\phi = 15^\circ$. The measured data are nicely reproduced by the AliRoot simulations for $\theta = 1^\circ$ (see Fig. 1). The measured data points for pions and electrons lie on two separate curves, roughly of $1/\sqrt{S/N}$ form. At a given S/N value, the resolution is worse for electrons as compared to pions. Since the S/N value at a given gas gain is about 60% larger for electrons, at normal operation conditions the resolution is very similar for both particle types. The data points without radiators shows better resolutions for electrons and lies on the same curve as the pion data,¹² while for pions the performance is similar with and

¹²The S/N value for electrons decreases without radiators due to the absence of energy deposit by TR.

without radiators. This indicates that the deterioration of the resolution in the case of electrons with radiators is connected with one of the following two processes:

- (i) Bremsstrahlung created in the radiator,
- (ii) transition radiation from the radiator.

The simulations reproduce the observed behavior well, implying that the Bremsstrahlung contribution is very small. The processes secondary to the TR absorption on the other hand, turn out to cause a significant deterioration of the detector resolution for the electrons. As described in Section 4.1, L-shell fluorescence X-rays are very common. They carry an energy of about 5 keV and their mean free path is about 0.4 cm in xenon. Their influence on the resolution is dominant; the influence of the range of photoelectrons and Auger electrons on the other hand is small,¹³ as well as the influence of K- and M-shell fluorescence X-rays. The former are high-energetic and generally escape from the region where the TR absorption takes place. The latter are low-energetic and their absorption length is too small ($\approx 100 \mu\text{m}$) to effectively influence the resolution.

6.2. Dependence on incident angle

Fig. 13 shows the position resolution σ_y and the angular resolution σ_ϕ as a function of the reconstructed angle ϕ_{rec} for two tail cancellation methods. The measured results are quantitatively reproduced by the AliRoot simulations. Only at small angles is the simulated resolution generally better than the measurements. This systematic deviation can be explained by a space charge effect [21]. At small values of the incident angle (perpendicular tracks) all electrons created along a track drift to the same anode wire spot¹⁴, leading

¹³This agrees well with our observation that a magnetic field of 0.14 to 0.56 T has no influence on the resolution. The tracks of photo and Auger electrons would be curled up in magnetic fields of that strength, which would lead to an improved resolution.

¹⁴If a magnetic field is applied, the angle ϕ where the space charge effect is largest is modified by the Lorentz angle ϕ_L (see Eq. (14)).

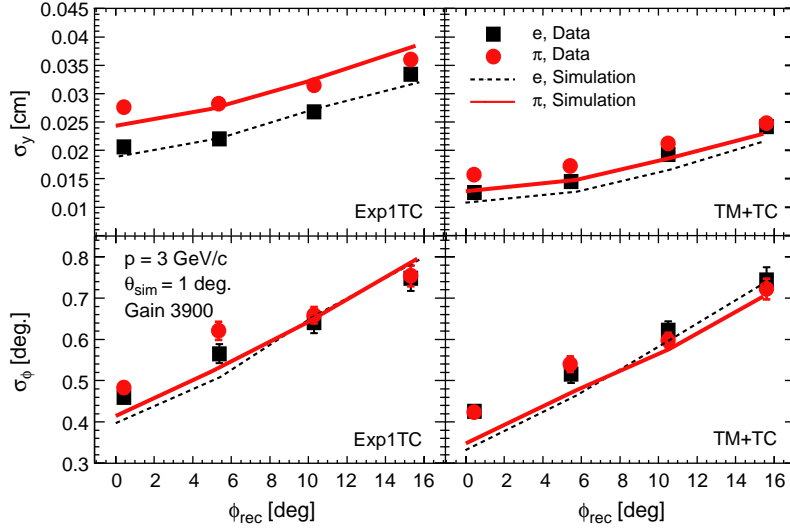


Fig. 13. Position resolution σ_y (upper panels) and angular resolution σ_ϕ (lower panels) as a function of the reconstructed angle for the Exp1TC (left panels) and TM+TC (right panels) methods. The radiators were mounted in front of the drift chambers and the simulated data correspondingly contains TR in the case of electrons.

to a buildup of positive ions around this wire spot. This reduces the effective gain and thus the S/N value for these conditions. As a consequence, we observe a deterioration of the resolution for small angles, which is not reproduced by the simulations, since no space charge effect is included.

For the Exp1TC method the measured position resolution is around $350 \mu\text{m}$ at $\phi_{\text{rec}} \approx 15^\circ$ and improves for smaller values of the incident angle. For the TM+TC method the position resolution is below $250 \mu\text{m}$ at all investigated angles. The angular resolution is around 0.7° at $\phi_{\text{rec}} \approx 15^\circ$ and below that value for smaller incident angles and both tail cancellation methods. While the TM+TC method does not improve the measured angular resolution—as was already mentioned—we observe a slight improvement in the simulated angular resolution. The observed performance is well within the requirements for the ALICE TRD that were listed in Section 1.

6.3. Dependence on drift velocity

The nominal drift velocity for the ALICE TRD of around $v_0 = 1.5 \text{ cm}/\mu\text{s}$ in the drift region was determined together with the sampling rate of

10 MHz to lead to a sufficiently large number of fit points for the track reconstruction ($N_{\text{fit}} \approx 20$, see Fig. 3). However, to provide more general results we also varied v_D and investigated its influence on the resolution of the detector. Fig. 14 shows the dependence of the position resolution σ_y and of the angular resolution σ_ϕ on v_D . In the measurements the average drift velocity $v_D^{\text{av}} \approx v_D$ can be extracted from the data using Eq. (1), if the incident angle of the beam is known. Values for v_D were varied by setting the drift voltage to 2.1 (nominal value), 2.4 and 2.7 kV, while keeping the anode wire voltage constant at 1.55 kV, corresponding to a gain of 3900. The two main contributions to the resulting resolution values are the lever arm of the fit (number of fit points) and the average amplitude per time bin. The number of fit points depends inversely on the drift velocity. The average amplitude per time bin is increased by a larger drift velocity, since more electrons reach the anode wires per time unit, leading to an increase of the S/N value. As a consequence we find, in Fig. 14, that a large drift velocity leads to a deterioration in the resolution due to the decrease in the number of fit points. Accordingly, the resolution also deteriorates for small drift velocities, due to the

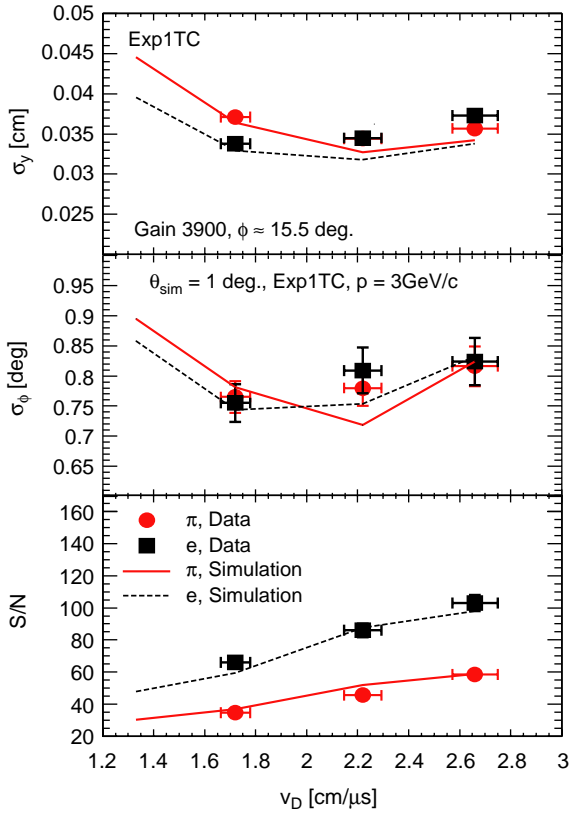


Fig. 14. Measured and simulated dependence of the detector performance on the drift velocity for electrons and pions. From top to bottom the position resolution σ_y , angular resolution σ_ϕ and signal-to-noise ratio S/N are shown. The drift velocity scan was carried out with radiators.

decrease of S/N . Our nominal conditions in the beam test—namely a drift voltage of 2.1 kV, corresponding to a drift velocity of around $v_D = 1.67 \text{ cm}/\mu\text{s}$ —turn out to be a good choice for our specific chamber dimensions and readout rate (10 MHz).

6.4. Dependence on momentum

In Fig. 15 we show the dependence of the resolutions σ_y and σ_ϕ on the beam momentum p . Generally, σ_y and σ_ϕ for pions improve for larger momenta, which is explained by the increased S/N value for larger momenta. The ratio S/N as a function of p is shown in the lower panel of Fig. 15. At $p \approx 0.56 \text{ GeV}/c$, corresponding to $\beta\gamma =$

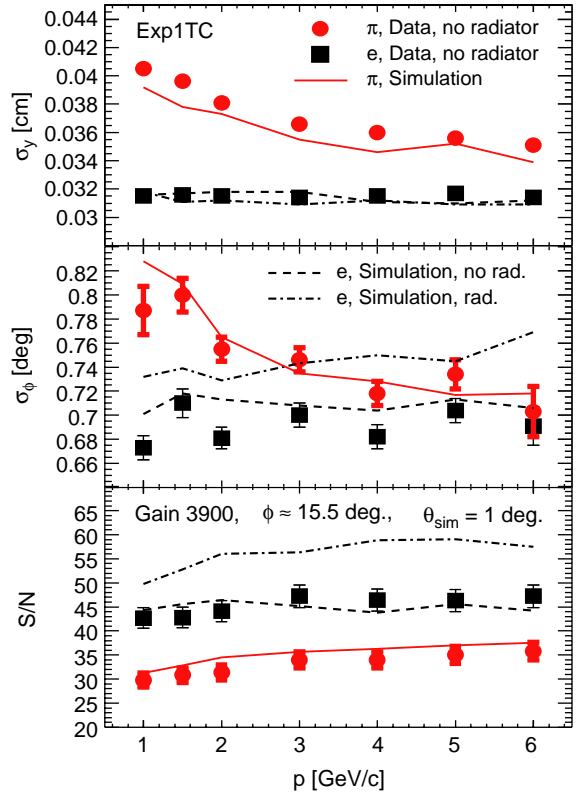


Fig. 15. Measured and simulated dependence of the detector performance on the particle momentum for electrons and pions. The position resolution σ_y , angular resolution σ_ϕ and S/N are shown (from top to bottom). The experimental momentum scan was carried out without radiators. However, here we added also simulated data with TR to demonstrate its momentum-dependent effect on the resolution of the electrons.

$p/(m_\pi c) \approx 4$ (where $m_\pi \approx 140 \text{ MeV}$ is the mass of the pion), pions are minimum ionizing; at larger momenta—especially in the momentum range of interest between 1 and 6 GeV/c —the ionization energy loss and thus the measured S/N value continuously increase [9]. Electrons already have a factor $\beta\gamma \approx 2000$ at $p = 1 \text{ GeV}/c$ momentum. Thus they are at the plateau of ionization energy loss. In the momentum range of interest, the S/N value is constant (with no radiators), leading to a constant resolution as a function of the momentum. The situation is changed with radiators, since at an electron momentum of $p = 1 \text{ GeV}/c$ the TR production sets in and at higher momenta the energy deposit due to TR and thus the S/N value

increase considerably. However, due to the effects described in Section 6.2 the performance is not improved by the larger energy deposit associated with TR, but deteriorated.

6.5. Performance in magnetic field

The ALICE TRD will be situated inside the large L3 barrel magnet with a magnetic field of 0.4 T. Since the electrons drift perpendicularly to the field, they will experience the Lorentz force that leads to a displacement of the clusters along the pad rows as a function of the drift time. For an electron produced at position (x_0, y_0, z_0) , where the y and z directions are perpendicular to the drift direction along x and the y direction is parallel to the wires (see Fig. 1), the new y position is given by

$$y = y_0 + \omega\tau(x - x_0), \quad \omega\tau = \tan \phi_L \quad (14)$$

where ϕ_L is the Lorentz angle. It is visible as an apparent inclination of the reconstructed track. If the track passing through the detector has an angle ϕ_0 , then the reconstructed angle ϕ_{rec} is given by

$$\phi_{\text{rec}} = \phi_0 - \phi_L + \delta\phi \quad (15)$$

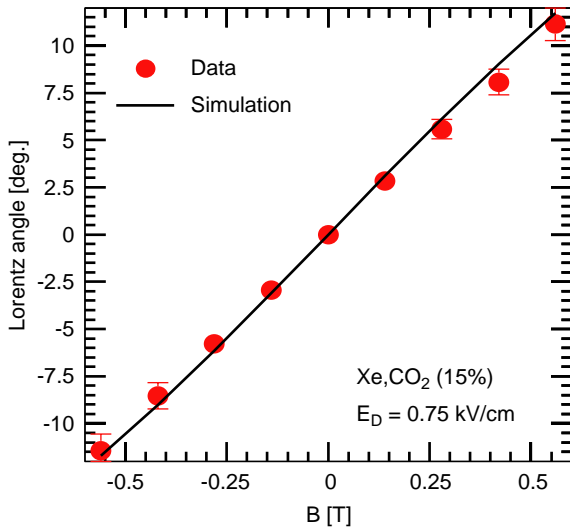


Fig. 16. Measured and calculated Lorentz angle for the Xe, CO₂ mixture as a function of the magnetic field B . The calculations were carried out with the MAGBOLTZ program. The drift field strength is $E_D = 0.75$ kV/cm.

where $\delta\phi$ is the error of the measurement. The Lorentz angle depends on the magnetic field strength and the drift velocity of the electrons. This dependence needs to be known to be able to reconstruct the original particle track and extract its inclination ϕ_0 .

We measured the Lorentz angle as a function of the magnetic field and of the electron drift velocity and compare the results to MAGBOLTZ [22] calculations (Fig. 16). For a magnetic field of 0.4 T and a drift field of 750 V/cm we find a Lorentz angle close to 8° .

In Fig. 17 we show the dependence of the resolution on the Lorentz angle ϕ_L . It is very similar to the dependence on ϕ_0 , which implies that the resolution depends only on the value of reconstructed angle ϕ_{rec} , and that additional effects due to the presence of the magnetic field are negligible. In Fig. 17 we also show data taken

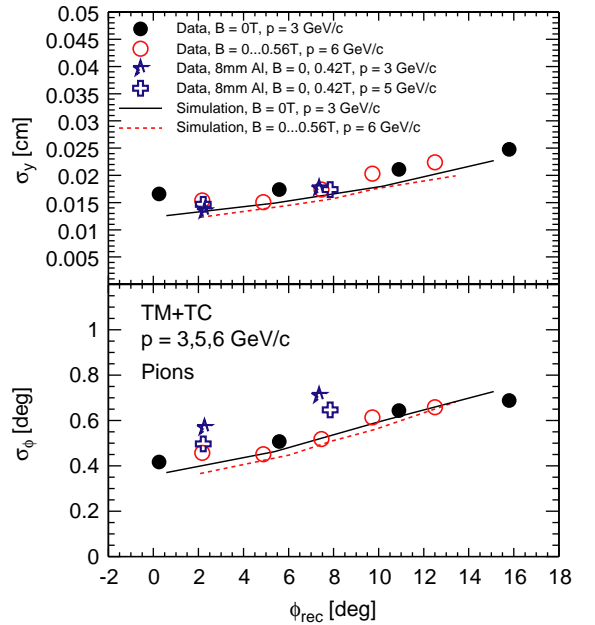


Fig. 17. Position resolution σ_y (top panel) and angular resolution σ_ϕ (lower panel) as a function of the reconstructed angle with and without magnetic field for pions. The symbols show the measurements, the lines show simulated data. In the data with magnetic field the actual incident beam angle was around $\phi_0 = 2.2^\circ$. The magnetic field dependent Lorentz angle is added to ϕ_0 following Eq. (15). We also show measured data taken with a 0.8 cm thick aluminum plate in front of the detectors (stars and crosses).

with a 0.8 cm thick aluminum plate in front of the detectors. This plate has a radiation length of about $0.9 X_0$, similar to that of four TRD layers. As expected, the resolution in σ_y is undisturbed, since it does not depend on external effects like multiple scattering. On the other hand, we find clear effects on σ_ϕ , evidencing a momentum dependent multiple scattering.

6.6. Performance compared to external track reference

Finally we show in Fig. 18 the position resolution of the detector with respect to a silicon strip detector, which is located a few centimeters in front of the investigated chamber. Let y_{DC} be the position of the center of the reconstructed track (at time bin 15, see Fig. 3) and y_{si} the position given

by the silicon telescope. Then $y_{si} - y_{DC}$ is a measure of the total position resolution of the drift chamber. This does however include the resolution of the silicon strip detector ($\approx 50 \mu\text{m}$) as well as the beam divergence ($\approx 0.1^\circ$) and external scattering effects. Fig. 18 shows a histogram of $y_{si} - y_{DC}$ for pions at $p = 4 \text{ GeV}/c$, at $\phi_0 \approx 15^\circ$, and for two tail cancellation methods. A Gaussian fit yields a position resolution of $376 \mu\text{m}$ for both methods, which is similar to the resolution extracted from the residuals for the same conditions.

7. Summary and conclusions

We have measured the performance of drift chamber prototypes for the ALICE Transition Radiation Detector (TRD) with respect to position and angular resolution. The detectors are drift chambers with cathode pad readout filled with the Xe, CO₂ (15%) mixture. For incident particle angles from 0 to 15° with respect to the wire normal we find a position resolution better than $300 \mu\text{m}$ (σ) and an angular resolution below 0.8° (σ). A systematic effect of about 0.36° at $\phi = 15^\circ$ is introduced by non-linearities: The discrete configuration of the wire grids in connection with the generally higher drift velocity in the amplification region introduces a modulation in the electron drift times, leading to a distortion of the space-time relation (non-linearity).

If a radiator is added to the drift chambers, transition radiation contributes to the energy deposit in the gas. Then the S/N is increased for electrons, but, nevertheless, the electron resolution is by about 7% worse in that case. L-shell fluorescence photons, which are produced in secondary processes after the absorption of the transition radiation photons, have an absorption length of about 0.4 cm in the xenon gas mixture. This smearing of the charge deposit around the actual track of the incident electrons introduces a considerable degradation of the position reconstruction performance for electrons.

The measurements are compared to simulations carried out with AliRoot, the ALICE event simulation and analysis framework. The

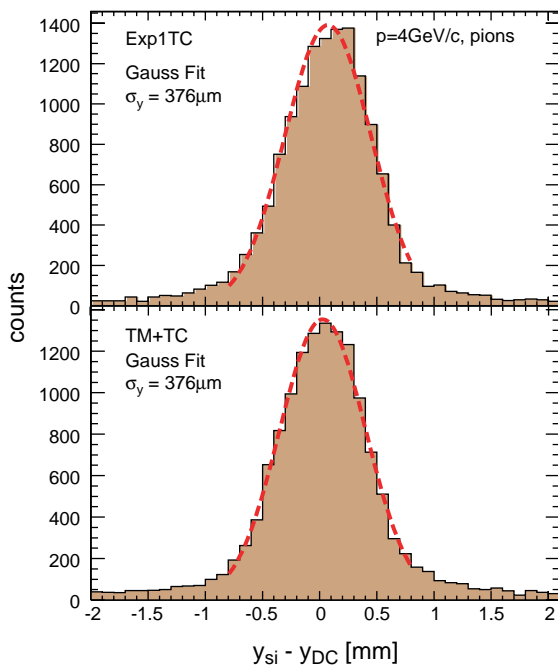


Fig. 18. Position resolution of the detectors with respect to a silicon strip detector for the Exp1TC (upper panel) and TM+TC (lower panel) methods for pions at $4 \text{ GeV}/c$. The extracted position resolution of $376 \mu\text{m}$ for both methods is for the reconstructed tracks at the center of the detector (time bin 15, $1.5 \mu\text{s}$ drift time, see Fig. 3). It includes the resolution of the silicon strip telescope ($\approx 50 \mu\text{m}$) as well as the beam divergence ($\approx 0.1^\circ$).

non-linearity of the electron drift was calculated with GARFIELD and included in the AliRoot code. Also a simplified picture of the secondary processes following the transition radiation absorption was added to AliRoot. The charge sharing between adjacent pads (pad response function) was calculated using an exact method (weighting field formalism). The performance of the detector is well understood and the position and angular resolution are within the requirements for the ALICE TRD. Our results—in particular the investigated systematic effects, the corrections applied, and the influence of the transition radiation—are of general interest also for other TRDs and/or other drift chambers with similar geometry, where a drift region is added to a multiwire proportional chamber, with the electron drift perpendicular to the wire planes.

Acknowledgements

We acknowledge A. Radu and J. Hehner for their skills and dedication in building our detectors and N. Kurz for his help on data acquisition. We would also like to acknowledge A. Przybyla for his technical assistance during the measurements.

References

- [1] G. Charpak, et al., Nucl. Instr. and Meth. 62 (1968) 262.
- [2] W. Blum, L. Rolandi, Particle Detection with Drift Chambers, Springer, Berlin, Heidelberg, 1994.
- [3] ALICE Transition Radiation Detector Technical Design Report, ALICE TDR 9, CERN/LHCC 2001-021; <http://www-alice.gsi.de/trd>.
- [4] A. Andronic, et al., Nucl. Instr. and Meth. A 498 (2003) 143.
- [5] A. Andronic, et al., Nucl. Instr. and Meth. A 523 (2004) 302.
- [6] B. Dolgoshein, Nucl. Instr. and Meth. A 326 (1993) 434.
- [7] O. Busch, et al., Nucl. Instr. and Meth. A 522 (2004) 45.
- [8] A. Andronic, et al., Nucl. Instr. and Meth. A 522 (2004) 40.
- [9] A. Andronic, et al., Nucl. Instr. and Meth. 519 (2004) 508.
- [10] O. Busch, et al., Nucl. Instr. and Meth. A 525 (2004) 153.
- [11] R. Brun, et al., Nucl. Instr. and Meth. A 502 (2003) 339; <http://aliweb.cern.ch/offline/>. We use AliRoot Version 4.02.05.
- [12] R. Brun, et al., GEANT3 User Guide, CERN, 1985; <http://wwwasd.web.cern.ch/wwwasd/geant/>. We use GEANT Version 3.21, CERN.
- [13] C.W. Fabjan, et al., Phys. Lett. B 57 (1975) 483.
- [14] J.E. Bateman, et al., Nucl. Instr. and Meth. 135 (1976) 235.
- [15] G. Charpak, F. Sauli, Nucl. Instr. and Meth. 152 (1978) 185.
- [16] F. Sauli, Principles of operation of multiwire proportional and drift chambers, CERN 77-09, CERN, 1977.
- [17] R. Veenhof, Nucl. Instr. and Meth. A 419 (1998) 726; <http://consult.cern.ch/writeup/garfield/>. We use GARFIELD Version 7.04, CERN.
- [18] J.S. Gordon, E. Mathieson, Nucl. Instr. and Meth. 227 (1984) 267; E. Mathieson, J.S. Gordon, Nucl. Instr. and Meth. 227 (1984) 277.
- [19] E. Mathieson, Nucl. Instr. and Meth. A 270 (1988) 602.
- [20] S. Ramo, Proc. IRE 27 (1939) 584.
- [21] A. Andronic, et al., Nucl. Instr. and Meth. A 525 (2004) 447.
- [22] S. Biagi, Nucl. Instr. and Meth. A 421 (1999) 234; <http://consult.cern.ch/writeup/magboltz/>. We use MAGBOLTZ Version 2.2, CERN.